8-14-2013

Multiscaffold DNA Origami Nanoparticle Waveguides

William P. Klein
Boise State University

Charles N. Schmidt
Boise State University

Blake Rapp
Boise State University

Sadao Takabayashi
Boise State University

William B. Knowlton
Boise State University

See next page for additional authors

Authors

William P. Klein, Charles N. Schmidt, Blake Rapp, Sadao Takabayashi, William B. Knowlton, Jeunghoon Lee, Bernard Yurke, William L. Hughes, Elton Graugnard, and Wan Kuang

Multiscaffold DNA Origami Nanoparticle Waveguides

William P. Klein,[†] Charles N. Schmidt,[†] Blake Rapp,[‡] Sadao Takabayashi,[†] William B. Knowlton,[†,‡] Jeunghoon Lee,[§] Bernard Yurke,[†,‡] William L. Hughes,[†] Elton Graugnard,[†] and Wan Kuang*[‡]

[†]Department of Materials Science and Engineering, [‡]Department of Electrical and Computer Engineering, and [§]Department of Chemistry and Biochemistry, Boise State University, Boise, Idaho 83725 United States

Ⓢ *Supporting Information*

ABSTRACT: DNA origami templated self-assembly has shown its potential in creating rationally designed nanophotonic devices in a parallel and repeatable manner. In this investigation, we employ a multiscaffold DNA origami approach to fabricate linear waveguides of 10 nm diameter gold nanoparticles. This approach provides independent control over nanoparticle separation and spatial arrangement. The waveguides were characterized using atomic force microscopy and far-field polarization spectroscopy. This work provides a path toward large-scale plasmonic circuitry.

KEYWORDS: *Self-Assembly, DNA nanotechnology, DNA origami, plasmonics, darkfield microscopy, atomic force microscopy*
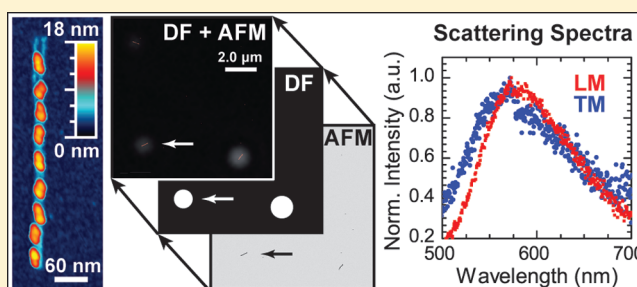
Driven by the promise of providing a relatively economical and massively parallel way of fabricating complex nanostructures, interest in DNA-directed self-assembly continues to grow.[1−4] By taking advantage of the specific binding between complementary DNA sequences, oligonucleotides can be formed into a variety of rationally designed shapes through a variety of processes including DNA origami,[5] molecular canvas,[6] DNA gridiron,[7] and designs that incorporate multiple scaffolds.[8] A primary driver of forming such nanoscale structures is the precise assembly of nanoparticles into well-controlled geometries in order to achieve novel material properties based on the collective behavior of the assembly.[9,10] For example, chains of closely spaced metal nanoparticles can guide electromagnetic energy below the diffraction limit by converting optical modes into nonradiating surface plasmons.[11−15] Waveguiding is made possible due to the resonant coupling between nanoparticles, and the resonant coupling frequency can be controlled by varying the nanoparticle diameter and the distance between adjacent nanoparticles.[16−18]

Metal nanoparticles can also be arranged into a variety of geometries that can fulfill the functions such as filters, directional couplers, beam splitters, and phase shifters.[19,20] Thus, precise control over nanoparticle size, spacing, and spatial arrangement offers the potential for a complete set of subdiffraction nanoscale optical components.

To enable efficient nanoparticle-based waveguiding, the plasmon modes of adjacent nanoparticles must be strongly coupled, which requires an interparticle gap smaller than the radii of the particles.[21,22] Previously, self-assembled plasmonic waveguides have been fabricated using meniscus force deposition[17,23] and direct DNA-based coupling.[10,24,25] These techniques allow the spacing between nanoparticles to be carefully controlled, enabling strong plasmon coupling, but they offer little control over spatial arrangement. For instance,

incorporation of multiple periodicities within a linear nanoparticle array would be extremely difficult, yet the arrangement of gold nanoparticles (AuNPs) into superlattices has been shown to allow precise engineering of waveguide mode dispersion.[26,27] A directed self-assembly method, such as DNA origami, has been shown to offer control over both interparticle gap and spatial arrangement,[28−30] however long linear superlattices incorporating multiple scaffolds have not yet been demonstrated."

Here, we report the directed self-assembly of AuNPs into linear semirigid superlattice arrays using single and multiscaffold DNA origami nanotubes. We demonstrate high-yield synthesis and high-fidelity to the designed target structure. Our design achieved a 14 nm center-to-center spacing between adjacent 10 nm diameter AuNPs for visible spectrum subdiffraction plasmonic waveguiding. Structural rigidity and minimal defects are critical factors for successful waveguide fabrication, and both were achived by cross-linking origami nanotubes into multiscaffold templates. Individual characterization of superlattice plasmonic waveguides revealed strong surface plasmon coupling in good agreement with simulations.

Plasmonic superlattice waveguides were formed by self-assembling AuNPs into linear arrays using six-helix DNA origami nanotubes with a designed diameter of 6 nm and length of 412 nm.[31] Figure 1 depicts the five plasmonic waveguide structures that were designed, synthesized, and characterized in this study. The 1xD1, 1xD2, and 1xT waveguide designs employ a single six-helix nanotube, as shown in Figure 1a−c, while the 2xD2 and 2xD3 designs employ two origami

Single Nanotube Designs
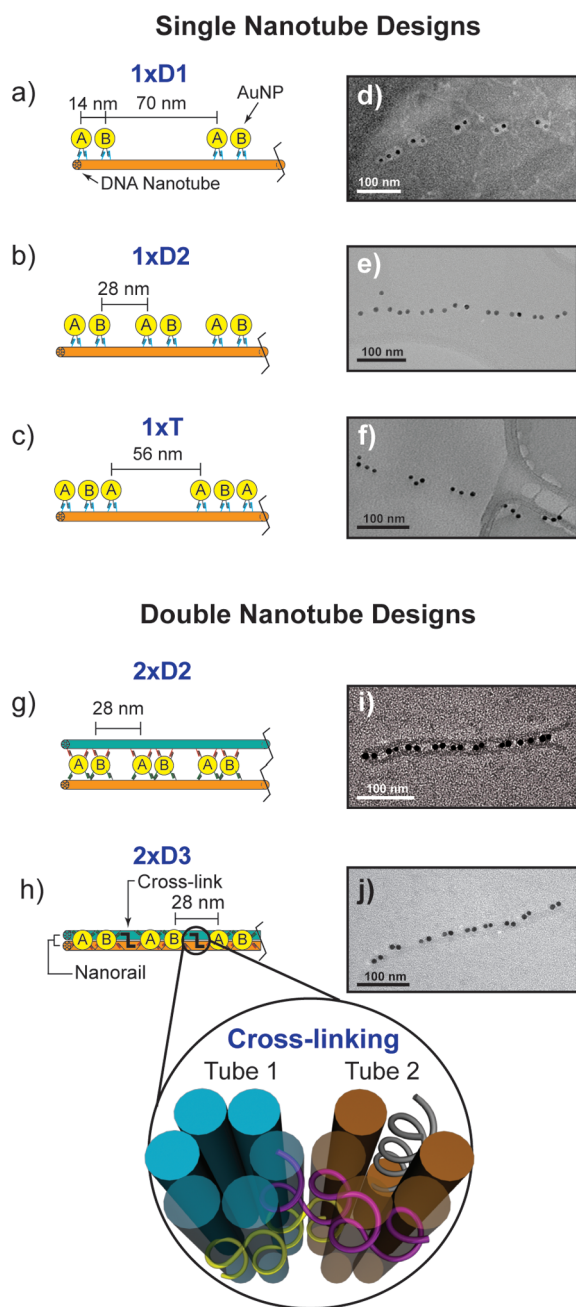

Double Nanotube Designs

Figure 1. (a−c) Schematics of the three single nanotube waveguides with 70, 28, and 56 nm periodicity between AuNP sets. (d−f) Negatively stained bright field TEM images of the waveguides for each corresponding design. (g,h) The double nanotube designs each consisted of two nanotubes to increase mechanically rigidity and the number of DNA sticky-ends that bind each AuNP to the tube. The 2xD2 design featured single 1xD2 nanotubes cross-linked through AuNPs, while the 2xD3 design incorporated 18 cross-linking ssDNA strands at nine locations, equally spaced along the waveguides. All designs incorporated a 14 nm center-to-center spacing between adjacent 10 nm diameter AuNPs. TEM images for double nanotube waveguides are shown in (i) and (j). A cross-section highlighting the routing of two cross-linking strands shown in yellow and purple. The blue and orange cylinders represent the DNA double helix. The staple strands have be omitted.

nanotubes, as shown in Figure 1g,h. To clarify, "1x" and "2x" describe the number of nanotubes involved in each design, while "D" and "T" indicate that the waveguide consisted of

superlattice arrays of AuNP dimers and trimers, respectively. 1xD1 and 1xD2 waveguides consisted of AuNP dimer sets periodically arranged at 70 and 28 nm spacings, respectively. 1xT consisted of AuNP trimer sets spaced by 56 nm. In all designs, the nanoparticle binding sites were separated by 14 nm within a dimer or trimer set.

Nanoparticle binding sites consisted of two identical 15 nucleotide (nt) sequences that extended from specific staple strands distributed along the nanotube axis. To prevent a single nanoparticle from hybridizing to two adjacent binding sites,[32] adjacent binding sites were designed with two unique sequences, denoted "A" and "B" in Figure 1. By modifying the location of the "A" and "B" binding sites on the nanotube, three different waveguides were synthesized. 1xD1 and 1xD2 waveguides each consisted of a periodic "AB" pattern, while 1xT waveguides consisted of a periodic "ABA" pattern. Ten nanometers diameter AuNPs were conjugated with thiolated single-stranded DNA (ssDNA) sequences complementary to "A" and "B" to enable site specific hybridization to the nanotubes.[28,30] The formation of 1xT waveguides required the hybridization of "B" AuNPs to the nanotube to occur before that of "A" AuNPs. This sequential hybridization procedure promotes steric hindrance and prevents "A" AuNPs from bridging two "A" sites over a "B" binding site. Design schematics, nanotube sequences, synthesis protocols, the AuNP conjugation process, and AuNP attachment yield are described in Supporting Information S1.

Negatively stained transmission electron microscope (TEM) images of successfully synthesized structures are shown to the right of each design schematic in Figure 1. As can be seen from the images, each target design was successfully synthesized, confirming the power of DNA-directed self-assembly in controlling both nanoparticle spacing and spatial arrangement. The TEM sample preparation is described in Supporting Information S2. Despite a high nanoparticle attachment yield, generally above 90%, characterization of the 1xD1, 1xD2, and 1xT waveguides revealed that AuNPs could fall on either side of the nanotube when depositing them on a substrate. This deviation from linearity was sufficient to cause the polarization dependence of the waveguides' scattering spectra to be poorly defined, as discussed below. Several examples are shown in Supporting Information S3. To better control the orientation and location of the AuNPs and to increase the mechanical rigidity of the waveguides, plasmonic waveguide arrays assembled on two DNA origami nanotubes were developed.

The 2xD2 waveguide arrays consist of two parallel nanotubes bound together by AuNPs as shown in Figure 1g. The structure resembles a ladder with AuNPs as the rungs of the ladder and the nanotubes as the legs. The structure was synthesized in the same manner as the 1xD2 structure; however, a modified AuNP to nanotube binding site concentration ratio was utilized. The AuNP to nanotube binding site ratios were 5:1 and 2:1 for the 1xD2 and 2xD2, respectively. Lowering the AuNP concentration promoted the formation of a laddered structures in which AuNPs were shared between two nanotubes. This approach added an additional constraint on AuNP placement and resulted in much higher nanoparticle linearity. However, the repeating binding sites on each tube led to the formation of waveguides with longitudinal misalignment between independent nanotubes, as shown in Supporting Information S4. The yield of well-formed waveguides was low using this approach.

An alternative multiscaffold approach is to intentionally construct nanoparticle templates by cross-linking two comple-
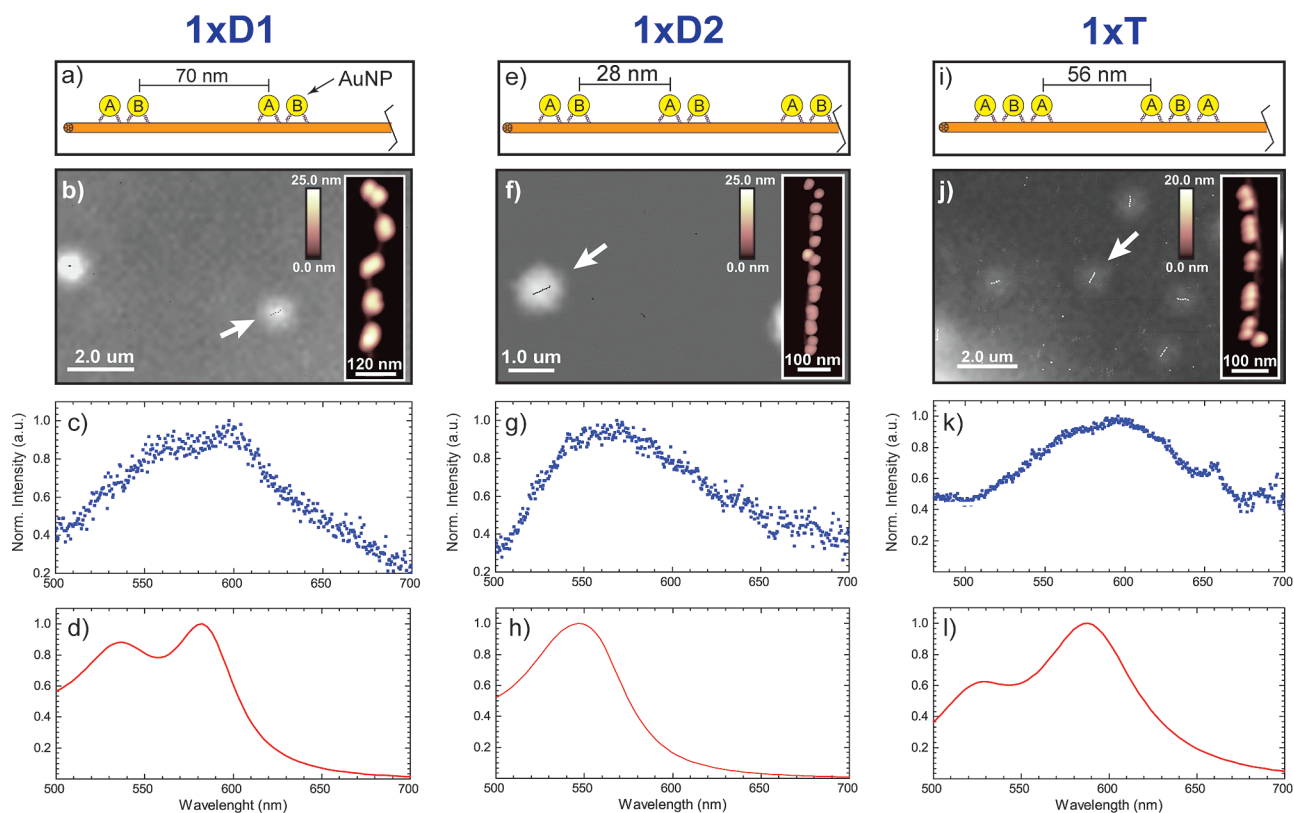
Figure 2. Plasmonic waveguide arrays assembled on a single six-helix bundle DNA origami nanotubes. The figure is divided into three columns, one for each of the waveguide array designs. The schematics for each design are shown at the top of each corresponding column. The combined AFM and darkfield images of the waveguides are shown in (b,f,j) with the inset of each image containing magnified AFM scans of the characterized waveguides. The bright halos surrounding the waveguides originate from the optical image and result from optical diffraction. The measured scattering spectra, (c,g,k), and the calculated scattering spectra, (d,h,l), of the waveguides are shown in the bottom two rows of the corresponding columns. The red shifts between the measured and calculated spectra are attributed to variations in the local refractive index of mica used in the experiments.

mentary nanotubes, as illustrated by the 2xD3 design in Figure 1h. Two nanotubes, designated tube 1 and tube 2, were designed to cross-link by modifying 18 of the original staple strands. An enlarged cross-section of the 2xD3 waveguide is shown and depicts the routing of the cross-linking strands shown in yellow and purple. The cylinders in the figure represent the double helix formed by the scaffolds and staple strands of the self-assembled waveguide. Staple strands and scaffold strands are not shown for clarity. Nine of the original 42 nt staple strands from one tube were lengthened by 14 nt to cross-link to the complementary nanotube, which has nine staple strands shortened by 14 nt. The same scheme was applied also in reverse to form a total of nine double intertube cross-links. Tubes 1 and 2 were synthesized and filtered separately and then hybridized to each other to form a single cross-linked structure, designated as 2xD3 and referred to as the "nanorail". The formation of the nanorail effectively doubled the number of sticky-ends per binding site to four, which improved the yield of well-formed waveguides in addition to eliminating the longitudinal misalignment between independent nanotubes that was observed with the 2xD2 waveguides. As can be seen in Figure 1j, the synthesized 2xD3 structures exhibited an high AuNP attachement yield and high nanoparticle linearity.

Once the yield of well-formed structures was sufficiently high (>90%), optical characterization of the waveguides was performed to investigate how different spatial arrangements

of AuNPs affected the surface plasmon resonance in each waveguide design. To prepare the self-assembled waveguides for topographical and optical characterization, the self-assembled waveguides were deposited onto atomically flat mica disks that were previously glued to a glass slide with optical epoxy as outlined in Supporting Information S5. To increase the scattering cross section and decrease the gap between pairs of the AuNPs, the AuNPs in some samples were enhanced using electroless deposition, as described in Supporting Information S6. All samples were completely dried with nitrogen gas prior to performing the atomic force microscopy (AFM) and darkfield microscopy characterizations.

During the AFM and darkfield characterization, low surface concentrations of ~10 waveguides per $30 \times 30 \ \mu m^2$ were found to be the most desirable for registration of individual waveguides. This low concentration greatly reduced excess scattering of light by neighboring waveguides. AFM characterization was performed in noncontact tapping mode using a Bruker Icon AFM equipped with a Bruker Fast-Scan head. The AFM scanning techniques are detailed in Supporting Information S7. During AFM characterization, four high-resolution $20 \times 20 \ \mu m^2$ noncontact mode height images were recorded in succession such that the images had approximately 2 μm of overlap to account for the thermal drift and moving the mechanical stage below its limit of resolution. The four images were post processed using Nanoscope Analysis (Bruker), WSxM,[33] and ImageJ[34] and
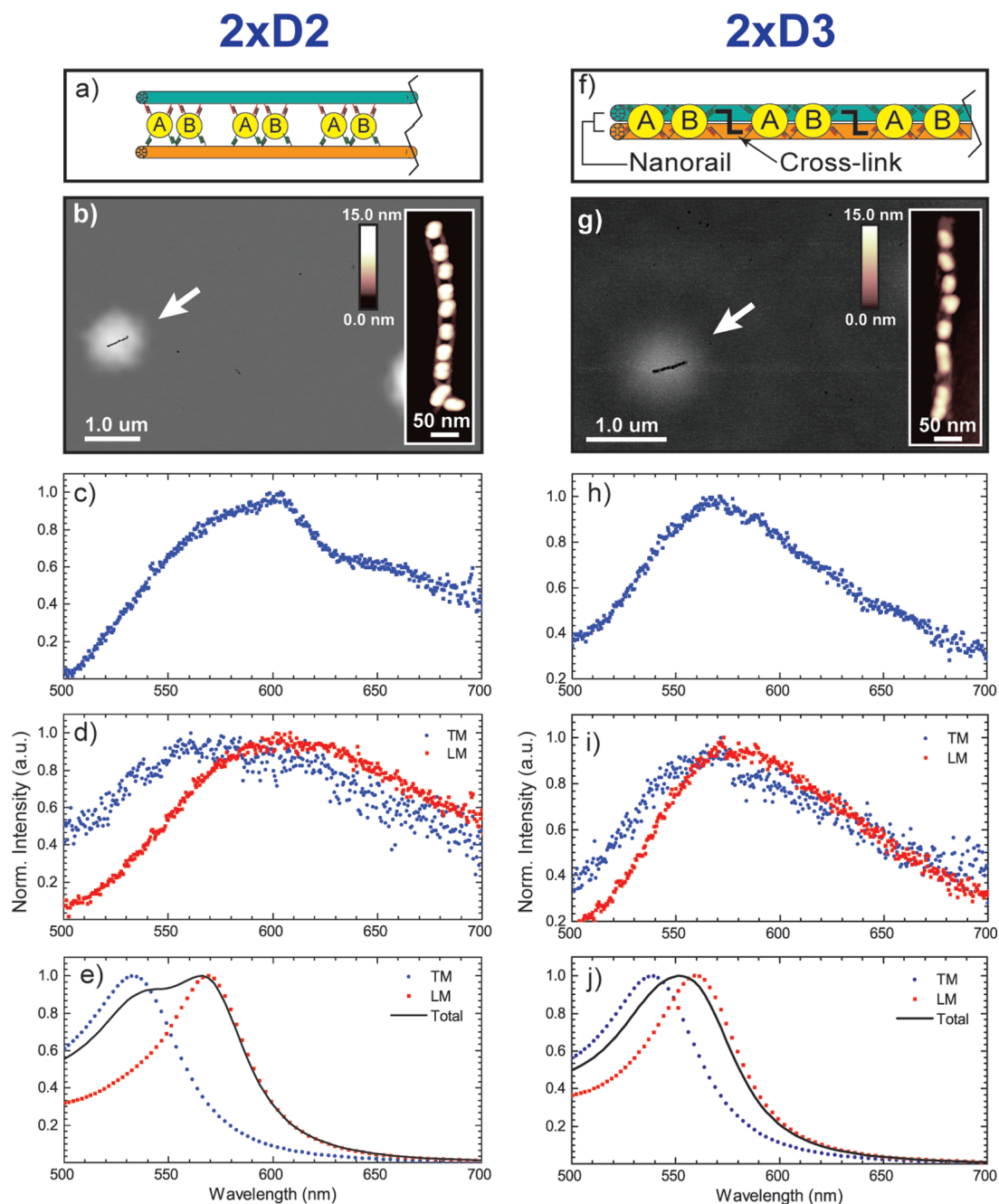
Figure 3. Plasmonic waveguide arrays assembled on two DNA origami nanotubes. (a−e) show results for the 2xD2 design and (f−j) show results for the 2xD3 design. The combined height AFM, darkfield, and magnified AFM scan of the characterized waveguides images of the waveguides are shown in (b,g). The measured scattering spectra of the waveguides shown in the AFM inset are shown in (c,h), and the polarized spectra are shown in (d,i). The calculated spectra of both LM and TM modes of the waveguides are shown as red squares and blue circles, respectively in (e,j). The LM and TM modes are collected with the polarizer parallel and perpendicular to the long axis of the waveguides, respectively. The spacings between the TM and LM modes of the collected polarized spectra agree with with the theoretical spacings.

then digitally combined into a single image covering approximately 30 × 30 μm^2. The independent AFM images were overlapped primarily using the unique pattern the individual waveguides created on the mica surface. Optical characterization of the waveguides was conducted using a spectrographic inverted darkfield microscope described in Supporting Information S8. By registration with fiducial reference marks, high-resolution AFM images and far-field optical spectra were collected from individual waveguides.

Figure 2a shows the schematic of a 1xD1 waveguide assembled on a single six-helix bundle DNA origami nanotube.

An AFM image overlaid with a transparent darkfield image is shown in Figure 2b. The two white halos surrounding the waveguides originate from the darkfield image and are the result of the scattering of light. The black dots located in the centers of the halos are the individual waveguides imaged by AFM. The magnified AFM image of the selected waveguide is shown in the inset of Figure 2b. The scattering spectrum of the waveguide under white light illumination was measured and calculated, as shown in Figure 2c,d, respectively. Additional measured scattering spectra can be found in Supporting Information S9. The numerical calculation was performed

with a finite element method using COMSOL,[35] assuming a nanoparticle radius of 6.3 nm, determined as the average particle radius from the AFM scan of the waveguide and a center-to-center spacing of 14 nm. The simulations assumed a constant value of 1.56 for the refractive index of mica for all calculations presented in this letter. The effective dielectric constant of Au is dispersive in the visible wavelength and was taken from Christy and Johnson.[36] The deviations observed in the measured scattering spectra from the calculated spectra are attributed to the difference in the local index of refraction of mica that varies depending on crystallographic orientation. The measured spectra were fit to a set of calculations, each of which assumed a particular value for the refractive index of mica. It was determined that the refractive index of mica to accurately model the measured spectra was in the range of 1.56 to 1.60, consistent with the index of refraction supplied by the manufacturer.[37] The refractive index of the DNA nanotubes was not considered in the simulations due to the fact that dsDNA has been shown to have a refractive index of 1.54 which is close to that of mica.[38]

The spacing between the AuNP dimer sets in 1xD2 waveguides (middle column of Figure 2) was 28 nm, as shown in the schematic. Although the waveguide shown in the inset of Figure 2f was fairly linear, few waveguides of this design possessed the linearity of this particular structure. The lack of linearity of the waveguides was identified as a common issue for waveguides assembled with a single DNA origami nanotube. In addition, the deviations of scattering spectra among individual waveguides are significant, as is shown in Supporting Information S9.

Figure 2i−l shows the results for waveguides consisting of AuNP trimers. A noticeable red shift was observed by comparing the scattering spectra of 1xT waveguides with 1xD waveguides. This result indicates that the trimer waveguides have a stronger longitudinal mode (LM) than the dimer waveguides, as expected. Additional spectra of 1xT waveguides can be found in Supporting Information S9. The spectrum calculated using a AuNP radius of 6.2 nm, determined as the average particle radius from the AFM scan of the waveguide, a mica refractive index of 1.56, and AuNP spacing of 14 nm for the 1xD waveguide is shown in Figure 2l.

The strong agreement between the measured and calculated spectra support the ability of DNA-directed self-assembly to form spatially complex superlattice arrangements of nanoparticles. As an additional assessment of the fidelity of DNA-directed self-assembly, the interparticle spacing of the single nanotube waveguide arrays was quantitatively determined by averaging the distance between adjacent nanoparticles contained within the dimer and trimer sets. In each design, the interparticle spacing within a dimer or trimer set was designed to be 14 nm. The measured interparticle spacing of the single nanotube waveguides were found to be 14 nm ($n = 101$), 16 nm ($n = 62$), and 13 nm ($n = 100$), for the 1xD1, 1xD2, and 1xT waveguides, respectively. All measurements had a standard deviation of 2 nm, which is close to the previously reported value of 1.4 nm for similar structures.[30] These results further support that DNA-directed self-assembly is capable of controlling nanoparticle spacing and thus interparticle gap.

Despite the control of AuNPs within dimer and trimer sets, in general, waveguides assembled on single DNA origami nanotubes were found to lack the mechanical rigidity required for the formation of highly linear waveguide arrays. By comparing calculated and measured scattering spectra, it was

determined that the measured spectra were produced by LM and transverse mode (TM) plasmon resonances of the AuNP dimers. Yet, the scattering spectra for both the 1xD1 and 1xD2 waveguides showed weak polarization dependency, as shown in Supporting Information S9. The deficiency of a well-defined polarization dependency of the scattering spectra is primarily attributed to the nonlinearity of the dimer and trimer sets on the waveguides. Furthermore, AuNPs would bind and lay on either side of the nanotube further compromising the optical properties of the waveguides, as previously described. These factors indicate that single DNA origami nanotubes are not suitable templates for fabricating linear plasmonic waveguides.

The linearity of the waveguides was greatly improved with the addition of a second nanotube orientated along the long axis of the structure, as illustrated by the 2xD2 and 2xD3 designs shown in Figure 3a,f. The 2xD2 waveguides consisted of two nanotubes linked by AuNP bridges, while the 2xD3 waveguides were cross-linked with ssDNA strands. Figure 3b−d shows AFM and optical results for one 2xD2 waveguide. The greatly improved alignment of the dimers due to the second nanotube resulted in well-defined polarized scattering spectra as shown in Figure 3d. The calculated polarized far-field spectra are shown in Figure 3e, which assumes a AuNP radius of 6.0 nm and a center-to-center distance of 14 nm. The spectral spacing between the TM and LM modes of the collected polarized spectra is in good agreement with the calculated values. Additional scattering spectra can be found in Supporting Information S9.

In general, the laddered waveguides possessed the mechanical rigidity and linearity required for the formation of desired linear waveguides. However, the yield of well-formed waveguides was difficult to control. The periodic arrangement of identical binding sites on the nanotubes led to the hybridization of AuNPs to nonequivalent sites of the two nanotubes, resulting in a longitudinal misalignment between independent nanotubes, as previously discussed. The low-yield problem of the 2xD2 waveguide was corrected by designing two complementary nanotubes that could hybridize to form the template for the 2xD3 waveguides.

TEM and AFM characterization of 2xD3 waveguide arrays confirmed a much greater yield (over 90%) of well-formed, linear waveguide structures. The results for the 2xD3 design are shown in Figure 3g−i. Complete AuNP attachment was observed and attributed to the 2-fold increase in the number of AuNP binding tethers (four tethers per binding site) that were incorporated into the structure.[39] The combined AFM and darkfield image is shown in Figure 3g, with a magnified view of the selected waveguide shown in the inset. The dimer alignment was greatly improved compared with waveguides assembled on a single origami nanotube. As a result, well-defined polarization dependent scattering spectra were obtained, as shown in Figure 3i. Additional spectral measurements of the 2xD3 waveguide arrays are provided in Supporting Information S9. The spectral spacing of 20 nm for the 2xD3 waveguides between the TM and LM modes of the collected polarized spectra agrees well with the calculated values. A radius of 5.4 nm and a center-to-center distance of 14 nm was used in the calculation in the spectra shown in Figure 3j. By comparing the scattering spectra from multiple 2xD3 waveguide measurements, as shown in Supporting Information S9, excellent conformance was observed, indicating a high fidelity to the waveguide design. Additional agreement to the designed structure was obtained from measurements of the interparticle

spacing of the double nanotube waveguides. Spacings were found to be 14 ± 2 nm ($n = 103$) and 13 ± 2 nm ($n = 102$) for the 2xD2 and 2xD3 waveguides, respectively, in perfect agreement with the designs.

In order to quantitatively analyze the linearity of the synthesized waveguides, AFM scans were analyzed for each waveguide design. Linearity was characterized by measuring the length of a line constructed tangent to the end of a waveguide and extending to the point where the curvature of the waveguide deviated from the center of the drawn line, as is shown in Supporting Information S10. Lines were constructed beginning from each end of the waveguide, and the two lengths were averaged to give the average linearity length for each waveguide. The 1xD1 waveguide had an average linearity length of 168 ± 78 nm ($n = 47$). Compared to an average linearity length of 257 ± 103 nm ($n = 51$) for the 2xD3 waveguide. Individual waveguides were declared linear if their average linear length exceeded 95% of the designed 412 nm length. The fraction of linear nanotubes was determined by summing the total number of linear waveguides by the total number of waveguides analyzed. The 1xD1 and 2xD3 waveguides' percent of linear waveguides were determined to be 41 and 63%, respectively. Use of three or four cross-linked nanotubes in a single waveguide are expected to increase the waveguide linearities further.

As a final comment, we note that the peak resonance wavelength of a waveguides strongly depends on the refractive index of its local environment. The calculated spectra are generally shifted 20 nm from those obtained by measurement, however the actual amount of wavelength shift depends on the actual index of refraction of the mica substrate below the waveguide. Red shifts of up to 40 nm depending on the surface area of the nanoparticles have been shown in simulations.[40] The spectral differences can also be attributed to the size distribution of AuNPs. The calculated far-field scattering spectra assume all the AuNPs have the same radius and are perfectly spherical. In reality, the AuNPs attached to the waveguide have a distribution of sizes and are not perfectly spherical. The AuNPs used in this study had a standard deviation in diameter of 1 nm and were >95% spherical.[41] The reduced sphericity causes a slightly enhanced resonance along the long axis of the particle.[42] This deviation in size distribution has been shown to cause broadening of both the TM and LM peaks and leads to red shifts of both TM and LM modes.[17] The calculated scattering spectra also assumed all the dimers to be in a completely linear configuration. Deviations in linearity of the waveguide would blue shift both the TM and LM peaks.

In summary, through DNA-directed self-assembly, we constructed linear plasmonic superlattice waveguide arrays with precise control of both interparticle gap and spatial arrangement, exhibiting well-defined optical properties in agreement with calculations. By conducting AFM and darkfield characterization on the same individual waveguides, we directly correlated structure and optical properties to show that the deviations of the orientations of AuNP dimer and trimer sets within the superlattice arrays have a significant impact on the polarization dependent scattering spectra. The use of a multiscaffold, two-nanotube nanorail structure greatly improved the mechanical ridgidity, and thus linearity, of the waveguides. These results indicate that with cross-linking of multiple DNA scaffolds, DNA origami can be used to fabricate relatively large and complex waveguiding structures.

AUTHOR INFORMATION

Corresponding Author

*E-mail: wankuang@boisestate.edu.

Notes

The authors declare no competing financial interest.

REFERENCES

(1) Modi, S.; Bhatia, D.; Simmel, F. C.; Krishnan, Y. *J. Phys. Chem. Lett.* **2010**, *1*, 1994−2005.

(2) Saaem, I.; LaBean, T. H. *Wiley Interdisciplinary Reviews. Nanomed. Nanobiotechnol.* **2013**, *5*, 150−162.

(3) Wang, F.; Willner, B.; Willner, I. *Curr. Opin. Biotechnol.* **2013**, *24*, 1−13.

(4) Linko, V.; Dietz, H. *Curr. Opin. Biotechnol.* **2013**, *24*, 1−7.

(5) Rothemund, P. *Nature* **2006**, *440*, 297−302.

(6) Wei, B.; Dai, M.; Yin, P. *Nature* **2012**, *485*, 623.

(7) Han, D.; Pal, S.; Yang, Y.; Jiang, S.; Nangreave, J.; Liu, Y.; Yan, H. *Science* **2013**, *339*, 1412−1415.

(8) Zhao, Z.; Liu, Y.; Yan, H. *Nano Lett.* **2011**, *11*, 2997−3002.

(9) Tan, S. J.; Campolongo, M. J.; Luo, D.; Cheng, W. L. *Nat. Nanotechnol.* **2011**, *6*, 268−276.

(10) Barrow, S. J.; Funston, A. M.; Wei, X.; Mulvaney, P. *Nano Today* **2013**, *8*, 138−167.

(11) Kreibig, U.; Vollmer, M. *Optical properties of metal clusters.* 1995; http://catalog.hathitrust.org/api/volumes/oclc/31331432.html (accessed Apr 2, 2013).

(12) Quinten, M.; Leitner, A.; Krenn, J.; Aussenegg, F. *Opt. Lett.* **1998**, *23*, 1331−1333.

(13) Krenn, J.; Dereux, A.; Weeber, J.; Bourillot, E.; Lacroute, Y.; Goudonnet, J.; Schider, G.; Gotschy, W.; Leitner, A.; Aussenegg, F.; Girard, C. *Phys. Rev. Lett.* **1999**, *82*, 2590−2593.

(14) Brongersma, M.; Hartman, J.; Atwater, H. *Phys. Rev. B* **2000**, *62*, 16356−16359.

(15) Maier, S.; Kik, P.; Atwater, H.; Meltzer, S.; Harel, E.; Koel, B.; Requicha, A. *Nat. Mater.* **2003**, *2*, 229−232.

(16) Busson, M. P.; Rolly, B.; Stout, B.; Bonod, N.; Larquet, E.; Polman, A.; Bidault, S. *Nano Lett.* **2011**, *11*, 5060−5065.

(17) Slaughter, L. S.; Willingham, B. A.; Chang, W.-S.; Chester, M. H.; Ogden, N.; Link, S. *Nano Lett.* **2012**, *12*, 3967−3972.

(18) Fan, J. A.; Bao, K.; Sun, L.; Bao, J.; Manoharan, V. N.; Nordlander, P.; Capasso, F. *Nano Lett.* **2012**, *12*, 5318−5324.

(19) Maier, S.; Kik, P.; Atwater, H. *Phys. Rev. B* **2003**, *67*, 205402.

(20) Yurke, B.; Kuang, W. *Phys. Rev. A* **2010**, *81*, 033814.

(21) Su, K.-H.; Wei, Q.-H.; Zhang, X.; Mock, J. J.; Smith, D. R.; Schultz, S. *Nano Lett.* **2003**, *3*, 1087−1090.

(22) Jain, P. K.; Huang, W.; El-Sayed, M. A. *Nano Lett.* **2007**, *7*, 2080−2088.

(23) Alexander, K. D.; Hampton, M. J.; Zhang, S.; Dhawan, A.; Xu, H.; Lopez, R. *J. Raman Spectrosc.* **2009**, *40*, 2171−2175.

(24) Storhoff, J. J.; Lazarides, A. A.; Mucic, R. C.; Mirkin, C. A.; Letsinger, R. L.; Schatz, G. C. *J. Am. Chem. Soc.* **2000**, *122*, 4640−4650.

(25) Barrow, S. J.; Funston, A. M.; GÃmez, D. E.; Davis, T. J.; Mulvaney, P. *Nano Lett.* **2011**, *11*, 4180−4187.

(26) Xiao, J.; Huang, J.; Yu, K. *Phys. Rev. B* **2005**, *71*, 045404−045404.

(27) Sweatlock, L. A.; Maier, S. A.; Atwater, H. A.; Penninkhof, J. J.; Polman, A. *Phys. Rev. B* **2005**, *71*, 235408.

(28) Ding, B.; Deng, Z.; Yan, H.; Cabrini, S.; Zuckermann, R.; Bokor, J. *J. Am. Chem. Soc.* **2010**, *132*, 3248−+.

(29) Pilo-Pais, M.; Goldberg, S.; Samano, E.; LaBean, T. H.; Finkelstein, G. *Nano Lett.* **2011**, *11*, 3489−3492.

(30) Kuzyk, A.; Schreiber, R.; Fan, Z.; Pardatscher, G.; Roller, E.-M.; Hoegele, A.; Simmel, F. C.; Govorov, A. O.; Liedl, T. *Nature* **2012**, *483*, 311−314.

(31) Bui, H.; Onodera, C.; Kidwell, C.; Tan, Y.; Graugnard, E.; Kuang, W.; Lee, J.; Knowlton, W. B.; Yurke, B.; Hughes, W. L. *Nano Lett.* **2010**, *10*, 3367−3372.

(32) Zhang, X.; Servos, M. R.; Liu, J. *J. Am. Chem. Soc.* **2012**, *134*, 7266−7269.

(33) Horcas, I.; G.-R., J. M.; C., J.; G.-H., J.; Fernandez, R.; Baro, A. M. *Rev. Sci. Instrum.* **2007**, *78*, 013705−8.

(34) ImageJ Home Page, http://rsb.info.nih.gov (accessed Apr 27, 2013).

(35) Luong, N.; Cheng, C.-W.; Shih, M.-H.; Kuang, W. *Appl. Phys. Lett.* **2012**, *100*, 181107−181107.

(36) Johnson, P. B.; Christy, R. W. *Phys. Rev. B* **1972**, *6*, 4370−4379.

(37) Ted Pella, Inc., http://www.tedpella.com (accessed Mar 23, 2013).

(38) Elhadj, S.; Singh, G.; Saraf, R. *Langmuir* **2004**, *20*, 5539−5543.

(39) Takabyashi, S.; et al. unpublished work.

(40) Kelly, K. L.; Coronado, E.; Zhao, L. L.; Schatz, G. C. *J. Phys. Chem. B* **2003**, *107*, 668−677.

(41) BBI Solutions, http://www.buybbi.com/Produxts_GoldColloid_1.aspx (accessed Apr 27, 2013).

(42) Billaud, P.; Marhaba, S.; Cottancin, E.; Arnaud, L.; Bachelier, G.; Bonnet, C.; Del Fatti, N.; Lerme, J.; Vallee, F.; Vialle, J.-L.; Broyer, M.; Pellarin, M. *J. Phys. Chem. C* **2008**, *112*, 978−982.